

Complex magnetic ordering and associated topological Hall effect in a two-dimensional metallic chiral magnet

Nyayabanta Swain, Munir Shahzad and Pinaki Sengupta

School of Physical and Mathematical Sciences, Nanyang Technological University, 21 Nanyang Link, Singapore 637371

(Dated: May 27, 2020)

Motivated by recent experiments on the observation of room temperature skyrmions in a layered heterostructure and subsequent demonstration of topological Hall effect in the same system, we have studied a minimal model of itinerant electrons coupled to local moments with competing interactions in an external magnetic field. Working in the limit of strong magneto-electric coupling where the fast dynamics of the electrons can be decoupled from the slow dynamics of the local moments (treated as classical spins), we analyze the multiple field induced magnetic phases and the associated electronic transport properties in these regimes. Our results help understand the microscopic origin of the observed phenomena and further provide crucial insight into unconventional magneto-transport in metallic chiral magnets.

I. INTRODUCTION

The observation of skyrmion phase in the helical magnet MnSi has led to a rapid growth in the study of non-collinear magnetic phases and associated magneto-electric phenomena¹. First postulated as a topologically protected solution to a class of non-linear sigma model in high energy physics², skyrmions arise in magnetic systems as spontaneously formed spin textures with non-trivial topology³⁻⁵. These spin textures are topologically protected against any deformations^{5,6} which make them attractive for practical applications^{7,8}. In magnetic switching devices, efficient coupling of electric currents to these spin textures lead to large spin-transfer torques that arise at very low current densities^{9,10}. These spin textures drive unusual phenomena such as magneto-electric effect for non-collinear magnetic orderings^{11,12} and topological Hall effect for non-coplanar arrangement of the spins^{13,14}. These spin textures are promising in magnetic memory devices, where memory bits can be packed denser and are more robust due to their topological nature¹⁵⁻¹⁷. Understanding the microscopic origin of these complex structures and their associated electronic properties is key for harnessing their unique functionalities for practical applications⁸.

Skyrmions arise in chiral magnetic systems from a competition between collinear magnetic order (driven by Heisenberg exchange and anisotropic interactions) and non-collinearity caused by Dzyaloshinskii-Moriya (DM) interactions. Theoretical studies, including Monte Carlo simulations, of the two-dimensional classical spin model demonstrated that in chiral magnets with strong DM interaction, skyrmions appear in the presence of a magnetic field^{3,18-25}. Following MnSi, skyrmions have been observed in bulk samples of other non-centrosymmetric $B20$ compounds²⁶ such as $\text{Fe}_{1-x}\text{Co}_x\text{Si}$ ^{27,28}, FeGe ^{29,30}, and MnGe ^{14,31,32} where intrinsic DM interaction drives non-collinear order. Skyrmions also have been observed in an insulating chiral-lattice magnet Cu_2OSeO_3 ³³. More recently, artificial heterostructures comprising of thin films of ferromagnetic materials and heavy metals with strong

spin orbit coupling (SOC) have emerged as a versatile platform for controllably generating skyrmions^{23,34}. Here broken inversion symmetry coupled with strong SOC generates an effective DM interaction at the interface which can be tuned over a wide range by careful material selection. Experiments on interfaces of Fe and Fe/Pd thin films on Ir(111) system have shown that atomic size skyrmions can be engineered with the help of higher-order interactions such as the ring exchange³⁵ or due to the presence of longer-range competing interactions¹⁶. Furthermore, innovative multi-layer stackings of Ir/Fe/Co/Pt thin films lead to the strengthening of interfacial DM interactions and resulting in small sized skyrmions as compared to the bulk chiral magnets^{36,37}. The effect of skyrmions on physical properties is most pronounced when their sizes are small. Hence we have used artificially large values of DM interaction that generates small, lattice scale skyrmions. Even though most experimental systems yield skyrmions that are much larger than the lattice constants – we believe similar effects will be observed in systems with large sized skyrmions, but in weaker forms.

Moving charge carriers in skyrmion hosting materials result in novel electrodynamics³⁸, and give rise to the topological Hall effect (THE)^{13,14,39-42}. In recent experiments^{36,37}, the emergence of THE accompanying the onset of the skyrmion phase is demonstrated in an artificial heterostructure.

THE is understood in the adiabatic limit to arise from Berry phase accumulated by electrons moving through a complex non-coplanar spin texture with strong magneto-electric coupling^{12,43-45}. As an electron moves through a skyrmion background, with its spin constrained to be aligned with the local moment at each point, it picks up a Berry phase^{43,44,46}. The gauge flux acts as a fictitious magnetic field acting on the electrons and maps the interaction of the electron *spin* and local moments to a magnetic field coupled to the *charge* of the itinerant electrons, analogous to quantum Hall systems on a lattice. The resulting Lorentz force that drives a transverse current which produces distinctive signatures in Hall conductivity that being promising for potential applications,

can be used to detect the presence of skyrmions^{12,38}.

In this paper, we study a metallic chiral magnet with itinerant electrons coupled to local moments. Working in the limit of strong magneto-electric coupling, the dynamics of the itinerant electrons and that of the local moments are decoupled. The magnetic properties are modeled by classical Heisenberg spins on a square lattice with ferromagnetic exchange and DM interactions. The ground state magnetic phases under an external magnetic field are calculated using large scale Monte Carlo simulations based on the Metropolis algorithm. We focus on various non-collinear magnetic phases stabilized on this lattice and their effect on the conduction electron motion via a coupled electron-spin model. Our results can be summarized as follows: (i) Competition between the ferromagnetic exchange and a strong DM interaction results in a spiral ground state at zero magnetic field. When an external magnetic field is applied, there is a transition to a skyrmion crystal (SkX) phase at a critical field, and eventually evolves to a fully polarized (FM) phase as the applied field strength is increased continuously. With increasing temperature, the SkX ground state melts to a skyrmion liquid (SkL) phase and eventually becomes a paramagnet at high temperature. (ii) The charge and spin topological Hall conductivities show quantized features in the SkX regime. In the ground state, topological Hall conductivity is finite only in the SkX phase, displaying a discontinuous transition at the spiral-SkX and SkX-fully polarized phase boundaries. However, at intermediate temperature, with increasing values of the applied field, the topological Hall conductivity varies continuously – rising from inside the spiral ground state, reaches a maximum in the skyrmion phase, and then decaying gradually as the phase changes to a fully polarized phase. These observations are in qualitative agreement with the experiments presented in Refs. 36 and 37, providing a plausible microscopic understanding of the underlying physical mechanism. Crucially, our results demonstrate that thermodynamic and transport properties in the skyrmionic phase (ground state or at finite temperatures) exhibit distinctive features that can complement the use of more complex imaging experiments to detect skyrmions.

The rest of the paper is organized as follows. In section II we discuss the models used in this study. In section III we describe the method and the observables we calculate. In section IV we discuss the detailed results of our work, followed by the summary in section V.

II. MODEL

We investigate the ferromagnetic Heisenberg model with additional DM interaction and external magnetic field on the square lattice. The Hamiltonian under consideration is given by,

$$\hat{\mathcal{H}}_c = -J \sum_{\langle i,j \rangle} \mathbf{S}_i \cdot \mathbf{S}_j - \sum_{\langle i,j \rangle} \mathbf{D}_{ij} \cdot (\mathbf{S}_i \times \mathbf{S}_j) - B \sum_i S_i^z \quad (1)$$

where $\langle i,j \rangle$ denotes nearest neighbors and J is the ferromagnetic exchange coupling. $\mathbf{D}_{ij} = D(\hat{\mathbf{z}} \times \hat{\mathbf{r}}_{ij})$, with D as the strength of the DM interaction and $\hat{\mathbf{r}}_{ij}$ is the unit vector connecting \mathbf{r}_i to \mathbf{r}_j . B represents the Zeeman coupling of the spin with the external magnetic field applied along the z -axis. The localized spins are treated as classical vectors with unit length ($|\mathbf{S}_i| = 1$).

Further, to study the properties of conduction electrons on the background of localized spin textures, we consider the Kondo lattice model given by,

$$\hat{\mathcal{H}}_e = - \sum_{\langle i,j \rangle, \sigma} (t_{ij} c_{i\sigma}^\dagger c_{j\sigma} + \text{H.c.}) - \mu \sum_i n_i - J_K \sum_i \mathbf{S}_i \cdot \mathbf{s}_i \quad (2)$$

where the first term is the kinetic energy, involving nearest neighbor hopping t_{ij} and $c_{i\sigma}^\dagger$ ($c_{i\sigma}$) is a creation (annihilation) operator of an itinerant electron at site \mathbf{r}_i with spin σ . μ in the second term is the chemical potential controlling the density of electrons. The final term is the Kondo interaction, which describes the coupling between the local moment \mathbf{S}_i to the electron spin operator $\mathbf{s}_i = \sum_{\alpha\beta} c_{i\alpha}^\dagger \vec{\sigma}_{\alpha\beta} c_{i\beta}$ at each site i .

III. METHOD AND OBSERVABLES

We study Hamiltonian (1) with classical Monte Carlo (MC) based on the Metropolis algorithm. We use periodic boundary condition on the square lattice of size $L \times L$ with $L = 32 - 96$ and lattice size increasing in steps of $\Delta L = 8$. Efficient thermalization is ensured by a simulated annealing procedure, where the MC simulation is started from a random spin configuration corresponding to high temperature ($T_{high} \sim 2J$), and then the temperature is reduced in steps of $\Delta T = 0.02J$, and $0.01J$ respectively to reach the lowest temperature of $T_{low} = 0.001J$, equilibrating the system at each temperature. The equilibrium state at T_{low} is used as the ground state for calculating physical observable. At each temperature, we use 5×10^5 MC sweeps for equilibration, and another 5×10^5 MC sweeps (in steps of 5000 sweeps) for calculating the observable in the ground state. Near the phase boundary, we start with the variational ground state, and heat the system using the Monte Carlo method to study its finite temperature aspect. As a result the meta-stable phases have been avoided in this regime.

Using the above approach, we explore the magnetic phase diagram of our model. The real space configurations of the localized spins are used to identify the different magnetic orderings. Using the equilibrium MC configurations, we compute physical quantities such as magnetization, static spin structure factor, scalar spin chirality *etc.* to characterize the magnetic phases and intervening phase transitions.

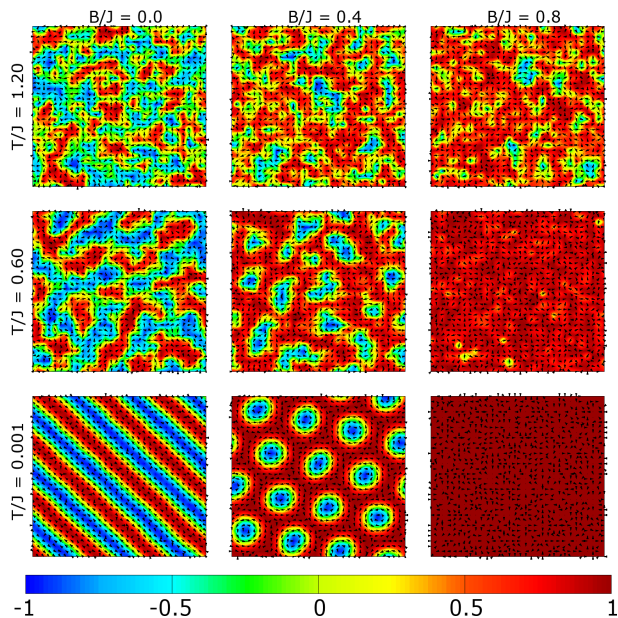


FIG. 1. Color online: Representative spin configurations ($\{\mathbf{S}_i\}$) obtained for different Zeeman coupling and temperature values from our Monte-Carlo simulation for $D = J$. The xy -components are represented by arrows in the xy plane, whereas the z -component is represented by the color scale.

We define magnetization as,

$$M = \frac{1}{N} \langle |\sum_i \mathbf{S}_i| \rangle.$$

The static spin structure factor is the Fourier transform of the equal-time spin-spin correlation, given by,

$$S(\mathbf{Q}) = \frac{1}{N} \sum_{i,j} \langle \mathbf{S}_i \cdot \mathbf{S}_j \rangle \exp[i\mathbf{Q} \cdot (\mathbf{r}_i - \mathbf{r}_j)]$$

The skyrmion number is used to identify the skyrmion phase, and can be inferred from the spin-chirality values, defined as,

$$\chi = \frac{1}{8\pi N} \langle \sum_i [\mathbf{S}_i \cdot (\mathbf{S}_{i+\hat{x}} \times \mathbf{S}_{i+\hat{y}}) + \mathbf{S}_i \cdot (\mathbf{S}_{i-\hat{x}} \times \mathbf{S}_{i-\hat{y}})] \rangle$$

In order to study the transport behavior, we consider Hamiltonian (2), and calculate the transverse conductivity using the Kubo formula⁴⁷,

$$\sigma_{xy} = \frac{ie^2\hbar}{N} \sum_{\sigma} \sum_{m,n \neq m} (f_m - f_n) \frac{\langle m | v_x | n \rangle \langle n | v_y | m \rangle}{(\mathcal{E}_m - \mathcal{E}_n)^2 + \eta^2}$$

where indices m and n represent the sum over all energy levels, N is the total number of sites, $f_{m(n)}$ is the Fermi-Dirac distribution function for energy $\mathcal{E}_{m(n)}$, $|m\rangle$ and $|n\rangle$ are single-particle eigenstates corresponding to energy \mathcal{E}_m and \mathcal{E}_n and η is the scattering rate of conduction electrons from the localized spins. v_x and v_y are

the velocity operators in \hat{x} and \hat{y} directions and can be expressed as,

$$v_{\mu} = \frac{i}{\hbar} \sum_{j,\sigma} (t_{j,j+\hat{\mu}} c_{j,\sigma}^{\dagger} c_{j+\hat{\mu},\sigma} - \text{H.c.}), \quad \mu = x, y$$

In addition to the total charge conductivity, we have also calculated the contributions from individual spin species. The non-coplanar spin texture exerts opposite forces on up and down spin electrons. As we shall discuss later, this is compounded by the overlap between the two spin species of electrons in the weak coupling regime, where the spin Hall conductivity behaves independently of the charge Hall conductivity. The transverse spin conductivity is given by an analogous Kubo formula that involves the spin current as,

$$\sigma_{xy}^S = \frac{ie}{4\pi N} \sum_{\sigma} \sum_{m,n \neq m} (f_m - f_n) \frac{\langle m | J_x | n \rangle \langle n | v_y | m \rangle}{(\mathcal{E}_m - \mathcal{E}_n)^2 + \eta^2}$$

where $J_x = \frac{1}{2} \{v_x, \text{diag}(\mathbf{S}_1 \cdot \sigma, \dots, \mathbf{S}_N \cdot \sigma)\}$ is the spin current operator.

IV. RESULTS

A. Magnetic properties

Local spin configuration: Fig.1 shows the local spin configurations for different magnetic field and temperature values at fixed $D/J = 1.0$. Since we are working with classical spins, a snapshot of the local spin configuration from the simulations (after equilibrium) provides a visual insight into the nature of the magnetic ground state. Our simulations are performed with classical spins of unit magnitude (i.e $|\mathbf{S}_i| = 1$) at each lattice point. We represent the localized spins as follows – S_{ix} and S_{iy} are represented by arrows in the xy plane, whereas S_{iz} is represented by a color scale (see figure 1). As there is no in-plane anisotropy in our model, the configurations obtained as the ground states from the Monte Carlo simulation have a companion configuration (obtained by rotating all the spins by $\pi/2$ along the z axis) with degenerate energy.

Fig.2(a) shows the energy of the spiral, skyrmion crystal, and ferromagnetic phases over the studied Zeeman coupling regime. Variational principle suggests that the ground state changes from a spiral phase, to a skyrmion crystal, and eventually to a field polarized ferromagnetic phase with increasing the Zeeman coupling. Further, we see the energy of the magnetic phase (corresponding to the lowest simulated temperature) obtained from our Monte Carlo simulation follows very closely the energy of the variationally obtained ground state phases; thereby confirming the correctness of the simulation process to reach the ground state. The critical magnetic field values and the phase transitions in the ground state are inferred from the level-crossing of the phases.

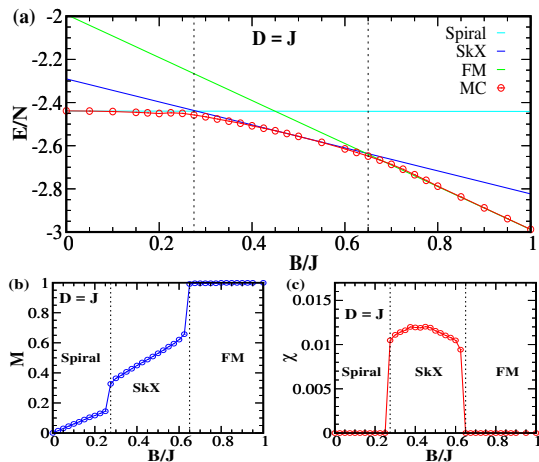


FIG. 2. Color online: (a) Energy per lattice site for different phases with changing Zeeman energy. This is compared with the energy of the configuration obtained from the Monte Carlo simulation at the lowest temperature. The ground state phases are determined by comparing the energies of the three static phases and the critical fields are identified as the points of energy level-crossing of the phases. The spiral phase at $B/J = 0.0$, the skyrmion crystal phase at $B/J = 0.5$ and a fully polarized phase are used as the reference states for carrying out the variational calculation. Comparison with the Monte Carlo data shows that the simulation results are consistent with the variational approach, providing an important benchmark for the numerical approach used in the study. (b) Magnetization calculated from the Monte-Carlo configurations in the ground state for different Zeeman field values. M increases monotonically with the magnetic field in the spiral and Skyrmion crystal phases and reached full saturation in the ferromagnetic phase, changing discontinuously at the phase boundaries. (c) Spin-chirality obtained from MC simulation for the ground state with varying applied field. $\chi = 0$ both in the spiral and the polarized phases, and $\chi > 0$ in the skyrmion crystal phase. The chirality also exhibits discontinuous jumps at the phase boundaries, consistent with the magnetization behavior.

We observe the following features. (i) For low magnetic fields ($0 \leq B/J < 0.27$), the ground state is a spin spiral phase. In this phase, the spins rotate about an axis in the XY plane with a pitch angle such that the wavevector $Q = 2\pi/\lambda \sim D/J$. With increasing temperature, thermal fluctuations randomize the spins, and above a critical temperature the state becomes a paramagnet. (ii) At intermediate field strengths ($0.27 \leq B/J \approx 0.65$) a skyrmion phase is obtained as the ground state. In this phase, the spin components S_{ix} and S_{iy} form an array of two dimensional vortices. This phase shows a periodic arrangement of individual skyrmions, and is known as the skyrmion crystal (SkX) phase. With increasing temperature, the periodic arrangement of skyrmions is lost to thermal fluctuations, and above a critical threshold, leads to a skyrmion liquid (SkL) phase. The skyrmions in this phase are elongated, strongly distorted, and distributed randomly in a background of field-polarized spins. Un-

like the low temperature SkX phase, the SkL phase survives till large temperature ($T \approx J$). The stability of the SkL phase is attributed to the topological nature of individual skyrmions. (iii) For high magnetic field values ($B/J \geq 0.65$), the skyrmion phase gets suppressed completely, and a ferromagnetic phase polarized along the field direction is obtained. Further increasing the magnetic field doesn't change the symmetry of this state. This polarized phase begins to randomize at large temperature ($T \approx J$) regime. A quantitative characterization of these different phases is obtained from the study of multiple observables as detailed below.

Magnetization: The behavior of magnetization M as a function of increasing magnetic field is shown in Fig. 2(b). In the ground state, M is vanishingly small in the absence of an external field. It increases slowly at small fields, with an almost linear dependence on B . At $B \approx 0.27J$, there is a jump in the value of the magnetization, signaling a discontinuous magnetic phase transition. In the field range $0.27J \lesssim B \lesssim 0.65J$, the magnetization increases with increasing external field. As $B \geq 0.65J$, M saturates to its maximum value indicating the appearance of a fully polarized phase. With increasing temperature, thermal fluctuations randomize the spin orientations and as a result reduce M .

Structure factor: A detailed understanding of the multiple magnetic phases is provided by the spin structure factor, $S(\mathbf{Q})$, which quantifies long range magnetic order in terms of prominent peaks (or dominant weight) in the momentum space. To isolate the effect of the longitudinal field on the spin correlations, we have calculated the structure factor components $S_{xy}(\mathbf{Q})$ and $S_z(\mathbf{Q})$ separately by using the xy -components and the z -components of the spins, respectively. We observe the following features (See Fig. 3), (i) In the spiral (low field) phase, both $S_{xy}(\mathbf{Q})$ and $S_z(\mathbf{Q})$ show two prominent Bragg peaks (seen as dominant weights in the color map) in the Q_x and Q_y plane. The two ordering momenta are not independent, but related by symmetry. This non-collinear long range ordered phase is specified by one wavevector (1- \mathbf{Q} state). (ii) In the SkX phase, $S_{xy}(\mathbf{Q})$ shows 6-peaks in the Q_x and Q_y plane – of these \mathbf{Q} 's, three are independent and for each peak there is another one related by symmetry. This state can be understood as a linear superposition of three spiral phases (each represented by two symmetry related wave-vectors), and is termed a 3- \mathbf{Q} state. The sharp peaks in these phase denotes a near-perfect close packed ordering of the skyrmions. $S_z(\mathbf{Q})$ shows 7-peaks in the Q_x and Q_y plane with the additional peak corresponding to $\mathbf{Q} = 0$ due to the uniform magnetization along the longitudinal direction. (iii) In the fully polarized ferromagnetic phase, $S_z(\mathbf{Q})$ shows a prominent peak at $\mathbf{Q} = 0$, and $S_{xy}(\mathbf{Q})$ shows no observable weight. (iv) The SkL phase, which stabilizes at finite temperature above the SkX phase, shows very weak, and diffused features in $S_{xy}(\mathbf{Q})$ in the Q_x and Q_y plane (not shown in the figure). This is due to the effect of thermal fluctuations on skyrmion configurations resulting in dis-

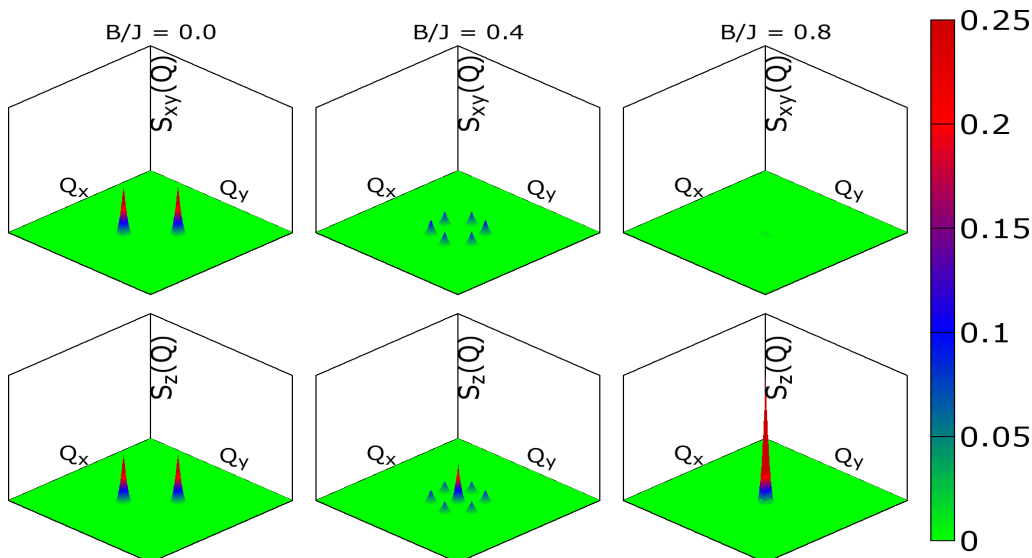


FIG. 3. Color online: Spin structure factor components $S_{xy}(\mathbf{Q})$ and $S_z(\mathbf{Q})$ in the ground state calculated for $Q_x, Q_y \in [-\pi, \pi]$ at indicated Zeeman field values for $D = J$.

torted skyrmions which lack long-range order and only show short range correlations.

Further we look into the variation of the peak of the structure factor component $S_{xy}(\mathbf{Q})$ with increasing temperature (see Fig.4). We observe that the structure factor weight reducing monotonically with increasing temperature across all phases. This is expected as increased thermal fluctuations randomize the magnetic phases, thus reducing the long-range correlation and eventually resulting in the loss of long-range order. The structure factor weight shows a stronger suppression beyond the critical temperature. We estimate the critical temperature, T_c , as the point of inflection of structure factor weight variation with increasing temperature. Our results indicate that the spiral phase shows a sharp reduction of the weight beyond T_c in contrast to the skyrmion phase, where the reduction is milder.

Spin chirality: One of the most interesting characteristics of complex non-coplanar spin textures is the non-zero chirality associated with them. Various spin texture are stabilized in the current system due to the interplay of the exchange interaction, the DM interaction and the applied magnetic field. To quantify the non-coplanarity of these spin textures we look into the scalar spin-chirality χ . Our calculation of χ gives the following results (see Fig. 2(c) and Fig. 5). (i) The low-temperature spiral phase is comprised of spins arranged in a non-collinear, but co-planar configuration. Accordingly, the $\chi = 0$ in this phase. With increased temperature thermal fluctuations gives rise to a small, non-zero value of χ in this regime. (ii) With the onset of the SkX phase at $B/J \approx 0.27$, the chirality increases discontinuously to a large value, reflecting the non-coplanarity of the spin configurations in this phase. The non-zero chirality arises entirely from the skyrmionic features. Indeed, the spin

chirality turns out to be a direct measure of the density of skyrmions. The chirality remains almost constant in the SkX phase as the density of skyrmions does not change. Upon the melting of the SkX into a SkL phase with increasing temperature $T \gtrsim T_c$, the density of skyrmions decrease rapidly. Consequently, the chirality exhibits a similar behavior. However, it is non-zero even at large temperature regime ($T \approx J$). (iii) As $B/J \geq 0.65$ at low temperature, chirality reduces due to increased polarization of the spins. For $B/J \geq 0.8$, $\chi = 0$, showing the fully polarization of the spins and the complete loss of non-coplanarity. At higher temperature, increased thermal fluctuations in this regime may lead to non-zero

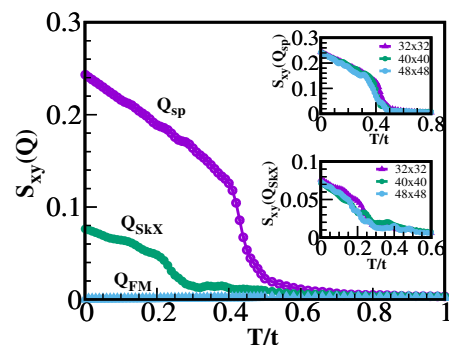


FIG. 4. Color online: Variation of the peak of the structure factor component $S_{xy}(\mathbf{Q})$ with temperature for $B/J = 0.0, 0.4$ and 0.8 , corresponding to the spiral, skyrmion and the field-polarized phases respectively. The point of inflection separates the low-temperature phase from the high-temperature phase and represents the critical temperature (T_c) for the respective phases. The insets show the variation of the structure factor peak for the spiral and skyrmion crystal phases for different system sizes.

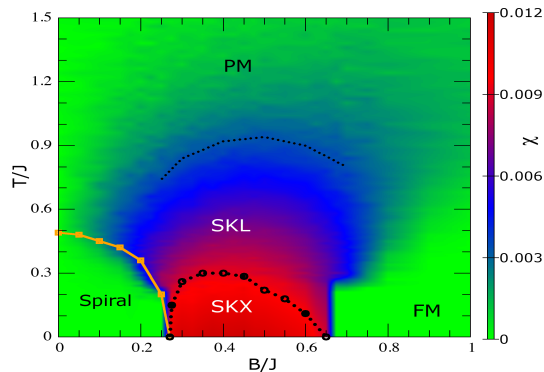


FIG. 5. Color online: Spin chirality, χ , obtained with our Monte-Carlo simulation for different Zeeman field values and temperatures at $D = J$. χ is non-zero in the skyrmion phase. Further, we highlight the different phases of our model here. At low temperature, thermal fluctuations lead to metastable states, resulting in narrow regions over which the phase transitions occur. The continuous line corresponds to a thermal phase transition from the spiral phase to a paramagnet brought by thermal fluctuations, and is inferred from the variation of the structure factor weight with increasing temperature (see Fig. 4). The dotted line separating the SkX phase from the SkL phase refers to a crossover highlighting the loss of long-range order in the SkL phase, but finite χ in both phases. The dotted line separating the SkL phase from the paramagnetic phase is also a crossover as indicated by the variation of Hall conductivity with increased temperature (see Fig. 10(b)). Further, the SkL phase is separated from the fully polarized FM phase by a crossover regime.

spin-chirality.

To summarize, Hamiltonian (1) exhibits a sequence of non-collinear magnetic ground states in an external magnetic field. In the absence of an external field, the interplay between the Heisenberg and DM interactions result in a spiral ordering of the localized moments. The spins rotate about an axis in the XY plane with a pitch angle that depends on the strength of the DM interaction. The periodicity of long range modulation of the spins is defined by a single momentum in both the longitudinal and transverse components of the static structure factor – a “1-Q” state. Increasing temperature in this phase leads to a paramagnetic phase above the critical temperature. At small Zeeman fields, the spiral ordering of the spins is maintained, but the spins acquire a continuously growing longitudinal component along the applied field. When the field reaches a critical strength, there is a discontinuous transition involving the nucleation of skyrmions and their simultaneous condensation into a self-organized close packed 2D crystal - the skyrmion crystal. The size of the skyrmions depends on the strength of the DM interaction relative to the Heisenberg interaction. The long range ordering of the spins is described by the superposition of three spiral orders and is characterized by three independent peaks in the longitudinal and transverse structure factors. The non-coplanarity of the spin texture is identified by a non-zero spin chirality. With

increasing temperature, the skyrmion crystal melts to a skyrmion liquid phase. The skyrmion liquid state – a thermally disordered phase with isolated and distorted skyrmions, is marked by a short range order arising from the spin textures of individual skyrmions. This is reflected in the form of diffused momentum dependence of the structure factor. The chirality also decreases as the density of skyrmions (which are the source of finite chirality) goes down. It is important to note that in the skyrmion-liquid phase, the suppression of the structure factor is much stronger than the suppression of the spin-chirality. In the ground state, with increasing magnetic field, the skyrmion crystal phase undergoes a continuous transition to a fully spin polarized state. However, at finite temperature, this will reflect in the form of a crossover of phases. The spin-chirality is zero in this phase.

In the skyrmion phase, χ can also be related to the discretized skyrmion number. We observe that the discretized skyrmion number is almost constant in the skyrmion crystal phase. With increasing temperature, this number decreases continuously in the SkL phase. The skyrmion number is zero both in the spiral phase and the fully field polarized phase.

For larger values of DM interactions, when the skyrmions are smaller and the density is larger, the chirality also increases proportionately. With varying DM interaction strength, we see χ showing the same qualitative behavior (See Fig. 6). However, we find the following important differences. (i) The skyrmion phase is stabilized over a larger Zeeman coupling regime for increased DM strengths. (ii) The skyrmion phase has larger chirality values with increasing DM strength, which suggest that there are more skyrmions (higher skyrmion number) in the SkX phase. This also agrees with the previous studies where increasing DM strength leads to smaller skyrmion size and hence increased skyrmion number.

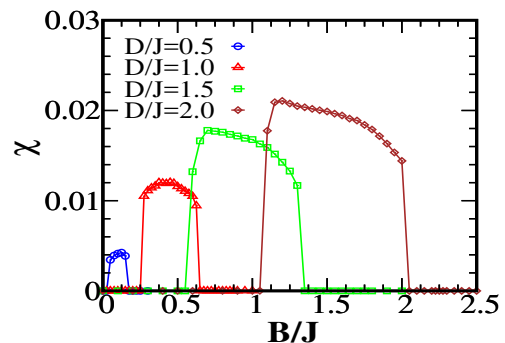


FIG. 6. Color online: Ground state spin chirality computed for different Zeeman field values and DM interaction strengths.

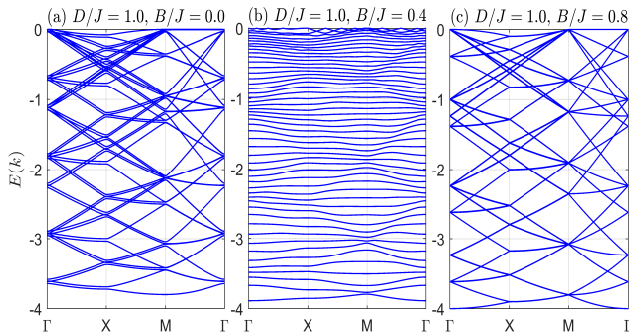


FIG. 7. Color online: Band structure of conduction electrons moving on the spin backgrounds of spiral, skyrmion and ferromagnetic phases for indicated values of DM interaction and magnetic field.

B. Electronic properties

Coupling to the local moments modifies the transport properties of itinerant electrons dramatically. For simplicity, we consider a single band of s -electrons interacting with the magnetic ordering via a Kondo coupling between the electron spin and the local moments. The dynamics of the electrons is fast compared to that of the localized classical spins. Consequently, at short time scales, the electrons effectively move in a static, but spatially varying magnetic field. Each local moment, \mathbf{S}_i acts as a local magnetic field whose action on the spin magnetic moment of the itinerant electrons \mathbf{s}_i is described by a Kondo-like interaction $J_K \mathbf{s}_i \cdot \mathbf{S}_i$. In comparison, the Zeeman energy due the external magnetic field coupled to the spin of the electron is small and shall be neglected. In the following, we discuss the effects of the different field induced spin textures on the energy dispersion and conductivity of the electrons.

Band structure : In the absence of an external field, the electron band structure consists of a single band with 2-fold spin degeneracy, and a band width $w = 8t$. There exist van Hove singularities at $\mathbf{k} = (0, \pm\pi)$ and $(\pm\pi, 0)$ where any interaction effects are maximized. A coupling to the spin texture increases the size of the unit cell in accordance with the magnetic unit cell. The Brillouin zone (BZ) is proportionately reduced and the bands are folded into the first BZ. A non-zero J_K lifts the spin degeneracy and the energy bands for electrons with spins parallel and anti-parallel to the local moments are shifted downwards and upwards, respectively. For sufficiently strong $J_K (> 8t)$, the spin parallel and anti-parallel bands are completely separated by a gap. In the limit of $J_K \gg t$, the electron spins are completely aligned with the local moments and Hamiltonian (2) reduces to an effective tight-binding model,

$$\hat{\mathcal{H}}_e = - \sum_{\langle i,j \rangle, \sigma} t_{ij}^{eff} (d_i^\dagger d_j + \text{H.c.}). \quad (3)$$

Where

$$t_{ij}^{eff} = t e^{ia_{ij}} \cos \frac{\theta_{ij}}{2}, \quad (4)$$

is the effective hopping matrix for the spin-parallel electrons between sites i and j and

$$a_{ij} = \arctan \frac{-\sin(\phi_i - \phi_j)}{\cos(\phi_i - \phi_j) + \cot \frac{\theta_i}{2} \cot \frac{\theta_j}{2}} \quad (5)$$

is the phase factor and θ_{ij} is the angle difference between two localized spins \mathbf{S}_i and \mathbf{S}_j . The spin anti-parallel electrons are described by a similar effective tight binding model with a different t_{ij}^{eff} and the two sectors are completely decoupled. The detailed effects of the magnetic orders in the different field induced phases are discussed below. For illustrative purpose, we have chosen an unphysically high value of the DM interaction to stabilize the magnetic order with short periodicity. This enhances the effects of electron coupling to local moments, allowing us to demonstrate them more effectively. Similar effects persist at smaller (and physically relevant) DM interaction strengths, but at a much smaller scale.

In this limit, the effective magnetic field produced by the spin texture couples directly to the charge of the electrons analogous to quantum Hall systems. The electron energy bands are modified depending on the nature of the underlying magnetic order.

To study the topological nature of the bands, we calculate the Chern number associated with each band as $C_n = \frac{1}{2\pi} \int_{\text{BZ}} \Omega_n^{(z)}(\mathbf{k}) d^2\mathbf{k}$ where, the Berry curvature is given by $\Omega_n^{(z)}(\mathbf{k}) = \partial_{k_x} A_n^{(y)}(\mathbf{k}) - \partial_{k_y} A_n^{(x)}(\mathbf{k})$ with $\mathbf{A}_n(\mathbf{k}) = -i \langle u_n(\mathbf{k}) | \nabla_{\mathbf{k}} | u_n(\mathbf{k}) \rangle$ as the Berry connection calculated from the eigenvectors $u_n(\mathbf{k})$ with eigenvalues $E_n(\mathbf{k})$ of the Hamiltonian 2. We focus on the band structure corresponding to different magnetic phases.

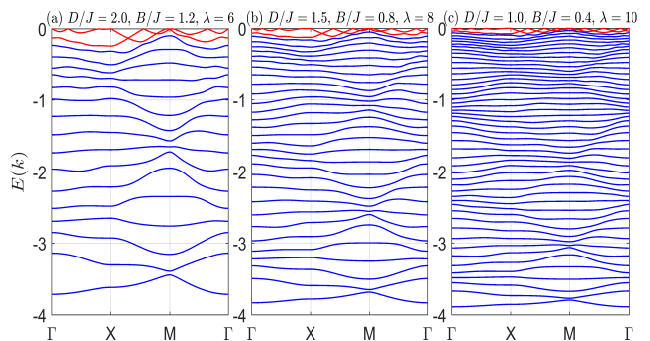


FIG. 8. Color online: Band structure of the conduction electrons on the skyrmion crystal background for indicated DM strengths and Zeeman coupling values. The bands, drawn in blue are separated from each other by a gap and have Chern number $C = -1$, whereas the bands drawn in red (two highest energy bands) are touching each other with Chern number equal to the sum of Chern numbers of the lower bands with opposite sign.

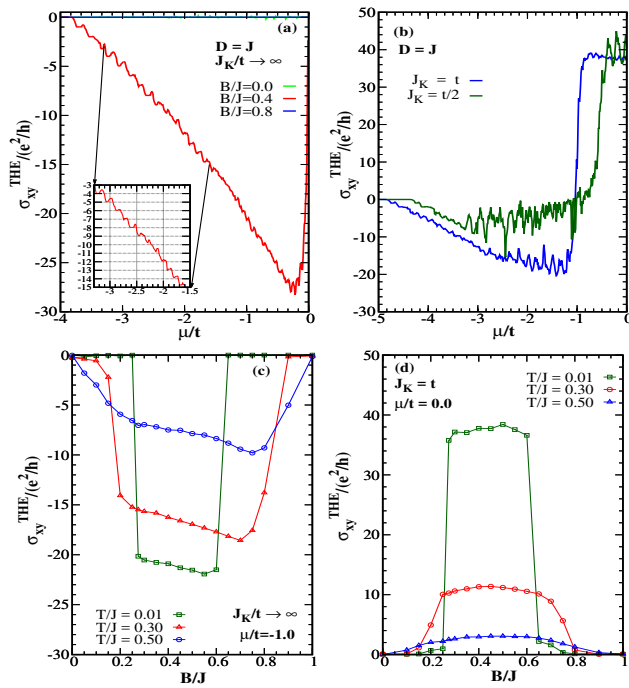


FIG. 9. Color online: (a)-(b) Behavior of the topological Hall conductivity with varying chemical potential in the ground state for $D = J$. Panel (a) shows the dependence of σ_{xy} on the chemical potential in the strong coupling limit ($J_K \rightarrow \infty$), for representative values of the applied field corresponding to spiral, SkX and ferromagnetic ground states. Panel (b) shows the effects of the strength of Kondo coupling on the variation of topological Hall conductivity with chemical potential for the SkX ground state. Results for three representative values of J_K/t are shown, corresponding to strong, intermediate and weak coupling strengths. For intermediate to weak coupling, the topological Hall conductivity is finite at $\mu = 0$, which is in a sharp contrast to the behavior for strong coupling. (c)-(d) Variation of the topological Hall conductivity at fixed chemical potential with changing magnetic field at different temperatures. Panel (c) corresponds to parameters $\mu = -t$ and $J_K \rightarrow \infty$, whereas, panel (d) corresponds to $\mu = 0$ and $J_K = t$. In the low temperature regime, σ_{xy} is finite only in the skyrmion phase and shows sharp jumps across the phase boundaries. For intermediate and high temperature regimes, σ_{xy} , increases rather continuously from the spiral to the skyrmion phase, and vanishes only deep in the polarized phase. While the conductivity at finite J_k shows qualitatively similar behavior to the $J_K \rightarrow \infty$ limit at low temperatures, the thermally induced σ_{xy} for spiral and ferromagnetic ground states are more pronounced for strong coupling strength.

(i) *Spiral phase*: The periodicity of the magnetic ordering at $D = 1.5J$ is observed to be $\lambda = 8$. This translates to a magnetic unit cell of size $\lambda \times \lambda$. The Brillouin zone (BZ) is reduced to $-\frac{\pi}{\lambda} \leq k_x, k_y < \frac{\pi}{\lambda}$. The band structure consists of $2\lambda^2$ bands that are completely separated for $J_K > 8t$. Fig.7 shows the band dispersion for the spin-parallel bands in the strong coupling limit along a high symmetry path in the 1st BZ, calculated using the effective tight binding model. For clarity of presentation,

only the bands with $E(\mathbf{k}) \leq 0$ are shown. The bands are modified from their non-interacting limit, but retain the large dispersion. No opening of bands gaps is observed.

(ii) *Skyrmion Crystal phase*: The effect of the spin texture is most pronounced in the skyrmion crystal phase, and has been studied in recent past with *ideal* skyrmions being constructed on different lattices^{43,44}. In the current work, we present results for interaction driven, *self consistently generated* skyrmion crystal phase. For the non-coplanar spin ordering of the skyrmions, the local moments around a plaquette subtend a finite solid angle at the center due to the spatially varying spin texture. This results in a finite Berry phase when an electron hops around a plaquette. In the strong coupling limit, the phase of the effective hopping, a_{ij} , can be associated with a vector potential acting on the itinerant electrons, analogous to quantum Hall systems. The flux of the corresponding fictitious magnetic field through each plaquette is given by $\Phi = (n_{sk}/\lambda^2)h/e$. The dispersion of itinerant electrons is strongly affected by this Berry phase. The bands get narrower. For the lower bands, a gap opens up between successive pairs of bands and each band acquires a finite Chern number (see fig. 8). However, the two uppermost bands are not complete gapped out; instead they touch each other at several \mathbf{k} -points in the BZ. Drawing on the analogy with quantum Hall systems, the bands can be described as dispersive Landau levels. For the (lower) block shown, each band carries a Chern number $C = -1$. Close to the van Hove singularity (VHS), two bands touch each other, and they carry a large Chern number $C = \lambda^2/2 - 2$ (where $\lambda \times \lambda$ is the size of the magnetic unit cell). Above it, the Chern number of each band changes sign. This has a dramatic effect on the behavior of the transverse conductivity, as discussed below.

The energy bands in the skyrmion crystal phase for different values of DM interaction are plotted in Fig.8, along the same path in the BZ. The plotted bands correspond to half of the number of bands (symmetric about $\mu = 0$), where conduction-electron spins are aligned with the local moments. Smaller values of D/J result in larger skyrmions. This leads to larger magnetic unit cells; correspondingly, the number of bands in the BZ increases. However, the qualitative features remain unchanged. The lower bands are separated from each other via a finite gap, have smaller bandwidths, and each carry a Chern number of $C = -1$; whereas the top two bands near $\mu = 0$ touch each other, and have a combined Chern number, $C = \lambda^2/2 - 2$.

(iii) *Fully polarized phase*: In the fully polarized phase, the electrons simply acquire a magnetic potential energy due to the uniform field produced by the local moments. The original symmetry of the lattice is restored and the number of bands reduces to two – one for each spin. The band structure in the reduced BZ is shown in Fig.7.

Hall conductivity: The coupling to local moments modifies the transport properties of itinerant electrons significantly in metallic magnets. The effect is most dra-

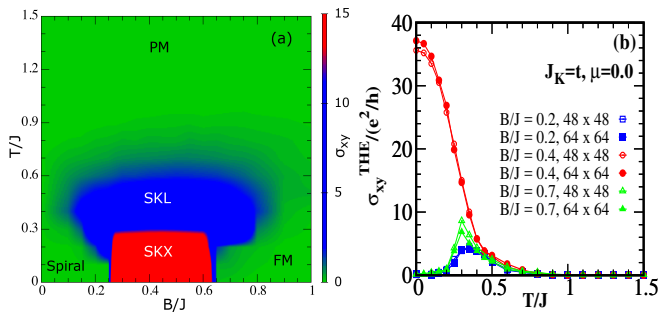


FIG. 10. Color online: (a) Behavior of the topological Hall conductivity with varying temperature and Zeeman field values for $D = J$. (b) Variation of the topological Hall conductivity with temperature for $B/J = 0.2, 0.4$ and 0.7 . For $B/J = 0.4$, the ground state is deep inside the SkX phase. With increasing temperature σ_{xy} reduces monotonically across the SkX and SkL phases, eventually vanishing at $T \approx J$. The temperature at which σ_{xy} reduces by 95% of the ground state value is identified as the crossover temperature. For $B/J = 0.2$ and 0.7 , the ground states are in the spiral and ferromagnetic phases, close to the ground state phase boundary with the SkX phase. For both these values of B/J , the THE displays a reentrant behavior. It increases from zero at low temperatures to a finite value for an intermediate range of temperature and eventually decreases to vanishing values at high temperatures. The data for different system sizes show negligible difference, confirming that the results are not artefacts of finite size effects.

matic in the transverse conductivity, especially when the underlying spin arrangement is non-coplanar. In a magnetic metal, the Hall resistivity consists of three contributions

$$\rho_{xy} = \rho_{xy}^{\text{NHE}} + \rho_{xy}^{\text{AHE}} + \rho_{xy}^{\text{THE}} \quad (6)$$

where NHE, AHE and THE refer to Normal, Anomalous and Topological Hall effects, respectively. The AHE appears in metals with a net magnetization due to spin-orbit coupling. On the other hand, the THE arises due to the real space Berry phase acquired by an electron moving in a non-coplanar spin texture. The phenomenon is best understood within the framework of the effective Hamiltonian (2) in the strong coupling limit ($J_K \gg t$). In this limit, the Berry phase acquired by an electron moving around a closed plaquette results in an effective flux threading each such plaquette that acts as a fictitious magnetic field and drives a Hall effect, whose origin is purely geometrical. In the present work, we focus on isolating the THE contribution to the transverse conductivity in the various field driven phases. Only the SkX and SkL phases exhibit finite THE. The spiral phase comprises of spins in a coplanar configuration whereas in the fully polarized phase, the spins are all aligned parallel to the applied field. The spin chirality vanishes for both of these configurations and consequently neither exhibit any THE. Fig. 9(a) shows the variation of the zero temperature Hall conductivity with changing the chemical potential for the spin aligned electrons in the strong cou-

pling limit for the lower half of the bands between the band minimum and the center of the band (the energies are shifted by a constant value so the the band extends over the range $[-4t, 4t]$). The conductivity for the upper half is symmetric about the band center. For the spiral and the fully polarized phases, the transverse conductivity remains zero, as discussed above. In the SkX phase, transverse conductivity exhibits a sequence of quantized plateaus analogous to quantum Hall plateaus. With increasing chemical potential, the value of σ_{xy}^{THE} decreases from zero at the band minimum in steps of e^2/h , in accordance with the Chern number $C = -1$ of the lower bands. In contrast to quantum Hall systems, the conductivity changes continuously, yet non-monotonically between the plateaus. This is a consequence of the finite dispersion of the electron energy bands (the bands are completely flat for quantum Hall systems). Close to the band center (which coincides with the VHS), the conductivity increases sharply, reflecting the large and positive value of the Chern number of bands close to the VHS. The quantization of the Hall plateaus is most pronounced for small skyrmion sizes where the lower bands are well separated. For larger skyrmions, the density of the bands increases and the energy extent of the conductivity plateaus decreases proportionately as does the energy separation between successive plateaus. This makes it difficult to resolve them in numerical simulations as effects of finite system size and fluctuations dominate.

At zero temperature only states below the Fermi energy, E_f contribute to the transport. When the Fermi energy lies within a plateau region, there is zero overlap between the current carrying states in the sample leading to the absence of backscattering processes. Thus the quantized value of σ_{xy} signifies the absence of backscattering amongst the states. If E_f is located within the band gap above any band, σ_{xy} is proportional to the winding number which is the sum of the Chern numbers of the filled bands. Below the band gap, the Hall conductance decreases, while it increases above the band gap. This is due to the fact that the sign of the Berry curvature is opposite between the two adjacent bands. This gives rise to a sawtooth shape of σ_{xy} , which becomes more pronounced when the skyrmion size is larger. With increasing skyrmion size (reducing the DM interaction), the qualitative behavior remains unchanged, but the detailed features get harder to resolve.

While the effects of large $J_K (\gg t)$ on ground state electronic transport has been extensively studied in the past (see Fig.9(a)), the effects of finite temperatures and intermediate values of coupling strength between itinerant electrons and localized moments ($J_K \approx t$) have remained largely unexplored. These are specially important for understanding experimental results, where the interest often lies in room temperature skyrmions, driven by the potential for practical applications. In the following we investigate these effects systematically and demonstrate that our results for transverse conductivity at finite temperatures agree well with experimental ob-

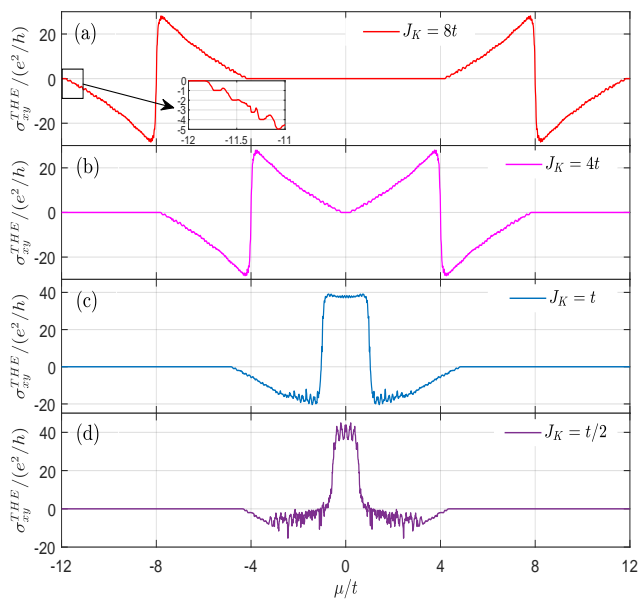


FIG. 11. Color online: The topological Hall conductivity as a function of varying chemical potential in the ground state of the skyrmion crystal phase ($B = 0.4J$) for different (finite) values of the Kondo-coupling. A finite THE is observed at $\mu = 0$ for intermediate to small coupling strengths ($J_K \lesssim t$), that is markedly absent at stronger couplings.

servations. Fig.9(b) shows the behavior of the topological Hall conductivity with varying chemical potential in the SkX phase in the ground state for finite values of J_K , together with that for large J_K . The most striking feature of the results for $J_K \lesssim t$ is the finite Hall conductivity at $\mu = 0$, which is in a sharp contrast to the behavior in the the $J_K \rightarrow \infty$ limit. This is because the electrons with spin aligned and anti-aligned to the local moments are not separated by a large gap for $J_K \lesssim t$. This results in multiple bands at the Fermi surface and a finite density of states at $\mu = 0$.

Fig.9(c)-(d) show the variation of the topological Hall conductivity with changing magnetic field for different temperatures. The field dependence of the topological Hall conductivity is qualitatively similar for all values of chemical potential as long as it is below the van Hove singularity. In the ground state ($T/J = 0.01$), we observe that $\sigma_{xy} = 0$ for a weak magnetic field (spiral phase) and a strong magnetic field (ferromagnetic phase), reflecting the absence of Berry phase in the coplanar (spiral) and collinear (ferromagnetic) magnetic orderings. In contrast, the non-coplanarity of the spin texture in the SkX phase induces a Berry phase in the conduction electrons which is reflected as a finite THE in this phase. The Hall conductivity exhibits a discontinuous transition at the spiral-SkX and SkX-fully polarized phase boundaries. At intermediate temperature, the Hall conductivity rises monotonically with increasing field values from well inside the spiral to the skyrmion phase. Similarly, at high magnetic fields, the transverse Hall conductivity

decreases in magnitude continuously and vanishes deep inside the fully polarized phase. Thermal fluctuations induce isolated spin clusters with non-zero chirality in the spiral and fully polarized ground state phases which results in a finite σ_{xy}^{THE} inside these phases. This behavior is qualitatively similar to the experimental observations^{36,37}. The precise nature of the skyrmion phase is different in the experimental system – in lieu of complete skyrmions, finite-length spin spirals with differently oriented axes are observed. However, a finite value of the net chirality confirms the topological character of the spin texture. The observed THE, which is finite in the skyrmion phase, exhibits a variation qualitatively very similar to our simulation results. This suggests that while a realistic microscopic model of the experimental system (that faithfully captures its multiple complexities) is likely to be extremely complicated, the simple Hamiltonian (1) represents a minimal model that correctly identifies the principal interactions and accompanying thermal effects that give rise to the experimental observations.

With increasing temperature thermal fluctuations destabilize the skyrmion phase further. As a result, the Hall conductivity reduces continuously and vanishes for $T \approx J$. The temperature at which the Hall conductivity reduces by 95% of the ground state value is identified as the crossover temperature (see Fig.10). In the spiral and the fully polarized phases, Hall conductivity is zero in the ground state. However, near the phase boundaries of the skyrmion phases, thermal fluctuations give rise to small, non-zero values of Hall conductivity even in the spiral and the fully polarized phases. An interesting consequence is a reentrant behavior of the topological Hall conductivity that is observed with increasing temperature for a spiral or fully polarized ground state close to the boundary with the skyrmion ground state. At low temperatures, the Hall conductivity vanishes due to zero net chirality for the ground state spin configuration. With increasing temperature, thermal fluctuations induce isolated spin clusters with non-vanishing net chirality which drives a finite THE. Finally, at high temperatures, any spin ordering is suppressed by large thermal fluctuations, and consequently, the topological contribution to the Hall conductivity vanishes.

We now turn our attention to the change in the behavior of transverse conductivity as the coupling between the conduction electrons and local moments is varied from strong to intermediate to weak. The results are shown in Fig.11. In the strong coupling regime, the plot consists of two well-separated blocks corresponding to electrons aligned parallel and anti-parallel to the local moments. The two segments exhibit similar features, but with opposite signs reflecting the opposite spin alignment of the electrons. The magnitude of the Hall conductivity increases in steps with increasing Fermi energy, before changing sharply from a large negative value to a large positive value as the Fermi level crosses the van Hove singularity for the lower energy band corresponding to

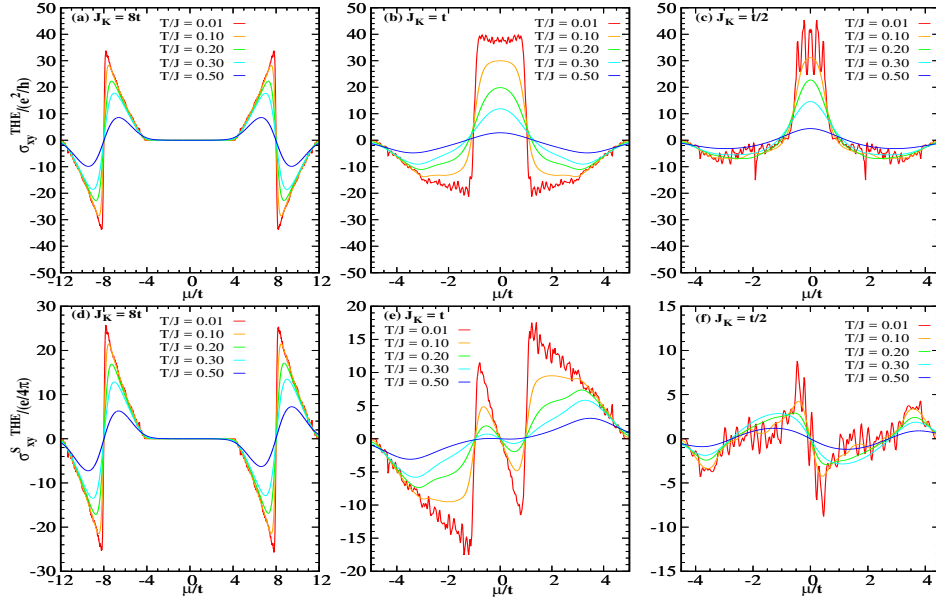


FIG. 12. Color online: Behavior of the topological charge Hall conductivity (a-c) and spin Hall conductivity (d-f) with varying chemical potential and temperature in the SkX phase ($B/J = 0.4$) for indicated J_K values.

spin parallel electrons. Further increase in Fermi energy sees the conductivity decrease in steps of e^2/h to zero at complete band filling for the spin-aligned electrons. The sudden change in the nature of the Hall conductivity is driven by the change in the nature of Fermi surface changes from electron-like to hole-like as the chemical potential crosses the van Hove singularity. The behavior for the upper band follows a similar behavior with opposite signs for the conductivity. The variation of the Hall conductivity with Fermi energy remains qualitatively similar for all $J_K > 4t$ where the two sets of energy bands are completely separated. For intermediate to weak coupling strengths ($J_K \lesssim t$), the two sets of bands start to overlap. The electrons are no longer strictly parallel or anti parallel to the local moments and the energy eigenstates comprise of contributions from both species. This Hall conductivity remains finite, and follows the same generic dependence on Fermi energy, but the conductivity plateaus are suppressed. The sharp change in the sign of σ_{xy}^{THE} remains unchanged since it arises due to the van Hove singularities and not the strength of the electron-local spin interaction.

Next we discuss the behavior of the charge and spin Hall conductivities in the skyrmion phase. While both the Hall conductivities are interlinked, we find interesting differences in their behavior in the skyrmion phase. Fig.12 shows the variation of the charge and spin Hall conductivities with changing chemical potential for different values of J_K . It can be clearly seen that the charge Hall conductivity is symmetric for positive and negative values of the chemical potential. However, this is not the case for the spin Hall conductivity. In the strong coupling limit ($J_K \gg t$), the energy bands for local spin-aligned and anti-aligned electrons are separated by a wide gap

and as a result, the charge and spin Hall conductivities follow one another closely since only one species of electrons contribute to the Hall conductivities. In the ground state, both the charge and spin Hall conductivities show quantized conductivity plateaus, exhibit a sharp jump and change in the sign as the chemical potential is tuned across the van Hove singularities. With increasing temperature we observe the disappearance of the conductivity plateaus and a systematic reduction in the conductivity values for any given chemical potential, which can be attributed to the thermal fluctuations. However, the change in sign of the conductivities at the van Hove singularities remains true. At intermediate and weak coupling, the local spin-aligned and anti-aligned bands overlap. The electron spin states hybridize and the spins of itinerant electrons no longer follow the local spins, i.e., the electrons spins are not simply aligned or anti-aligned to the local moments. The energy eigenstates have finite overlap with both electronic spin states. As a consequence, the charge and spin Hall conductivities are decoupled from each other. As observed for $J_K \gg t$, both the ground state, charge and spin Hall conductivities exhibit quantized conductivity plateaus separated by non-monotonic variation as the chemical potential is tuned, and exhibit a sharp jump and change in the sign as the chemical potential is tuned across the van Hove singularities. However, in a sharp contrast to the $J_K \gg t$ regime, for $J_K \leq t$, the charge Hall conductivity is finite at $\mu = 0$. This can be explained due to the existence of large density of states at $\mu = 0$ in the $J_K \leq t$ regime. The spin Hall conductivity vanishes at $\mu = 0$ irrespective of the J_K/t value. With increasing temperature the conductivity plateaus disappear and the conductivity values reduce gradually for a given value of the chemical poten-

tial.

V. SUMMARY

We have studied the emergence of field induced skyrmions in a chiral magnetic system and their effects on electron transport. Our results show that the interplay of ferromagnetic exchange and DM interaction in the presence of external magnetic field gives rise to several interesting magnetic phases, including the non-collinear spiral and the non-coplanar skyrmion phases. The nature of spin textures in these phases and the associated phase transitions are analyzed in detail with varying magnetic field and temperature. In the ground state, the Skyrmion phase consists of a regular array of Skyrmions forming a Skyrmion crystal. With increasing temperature, the Skyrmion crystal melts and over a finite range of temperature, the periodic array of regular Skyrmions is replaced by a random distribution of distorted spin chiral configurations. We term this phase Skyrmion liquid. Finally at high temperatures, the Skyrmion liquid melts to a paramagnetic state. Both the skyrmion crystal and liquid phases are shown to possess non-trivial spin-spin correlations and finite spin chirality. Complementing the magnetic properties, we have studied the band structure and the transport properties of itinerant electrons coupled to

different magnetic phases. The skyrmion phases exhibit a topological Hall effect and show finite charge and spin Hall conductivities, driven by the coupling of the itinerant electrons to the non-coplanar spin texture that generates a real space Berry curvature and associated effective local magnetic field. We have studied in detail the variation of these quantities with changing temperature, carrier density and the tuning of the coupling between itinerant electron and localized spin. The appearance of conductivity plateaus in the transverse conductivity in the skyrmion crystal phase is discussed in detail, including an understanding of the unusual behavior in the vicinity of van Hove singularities. The effects of finite band dispersion on transverse conductivity are also analyzed. Our results are expected to help in identifying materials exhibiting skyrmion phases based on magnetic and transport properties complementing the currently used complex imaging techniques.

ACKNOWLEDGMENTS

We acknowledge use of the HPCC cluster at NTU, Singapore and the NSCC ASPIRE1 cluster in Singapore for our numerical simulations. The work is partially supported by Grant No. MOE2014-T2-2-112 of the Ministry of Education, Singapore.

-
- ¹ S. Mühlbauer, B. Binz, F. Jonietz, C. Pfleiderer, A. Rosch, A. Neubauer, R. Georgii, and P. Böni, *Science* **323**, 915 (2009).
 - ² T. Skyrme, *Nucl. Phys.* **31**, 556 (1962).
 - ³ A. N. Bogdanov and U. K. Rößler, *Phys. Rev. Lett.* **87**, 037203 (2001).
 - ⁴ U. K. Rößler, A. N. Bogdanov, and C. Pfleiderer, *Nature* **442**, 797 (2006).
 - ⁵ N. Nagaosa and Y. Tokura, *Nat. Nanotech.* **8**, 899 (2013).
 - ⁶ J. Hagemeyer, N. Romming, K. von Bergmann, E. Y. Vedmedenko, and R. Wiesendanger, *Nat. Commun.* **6**, 8455 (2015).
 - ⁷ R. Wiesendanger, *Nat. Rev. Mater.* **1**, 16044 (2016).
 - ⁸ A. Fert, N. Reyren, and V. Cros, *Nat. Rev. Mater.* **2**, 17031 (2017).
 - ⁹ F. Jonietz, S. Mühlbauer, C. Pfleiderer, A. Neubauer, W. Münzer, A. Bauer, T. Adams, R. Georgii, P. Böni, R. A. Duine, K. Everschor, M. Garst, and A. Rosch, *Science* **330**, 1648 (2010).
 - ¹⁰ A. Fert, V. Cros, and J. Sampaio, *Nat. Nanotech.* **8**, 152 (2013).
 - ¹¹ Z. Wang, D.-K. Ki, H. Chen, H. Berger, A. H. MacDonald, and A. F. Morpurgo, *Nat. Commun.* **6**, 8339 (2015).
 - ¹² B. Göbel, A. Mook, J. Henk, and I. Mertig, *Phys. Rev. B* **99**, 060406 (2019).
 - ¹³ A. Neubauer, C. Pfleiderer, B. Binz, A. Rosch, R. Ritz, P. G. Niklowitz, and P. Böni, *Phys. Rev. Lett.* **102**, 186602 (2009).
 - ¹⁴ N. Kanazawa, Y. Onose, T. Arima, D. Okuyama, K. Ohoyama, S. Wakimoto, K. Kakurai, S. Ishiwata, and Y. Tokura, *Phys. Rev. Lett.* **106**, 156603 (2011).
 - ¹⁵ A. Fert, in *Metallic Multilayers*, Materials Science Forum, Vol. 59 (Trans Tech Publications, 1991) pp. 439–480.
 - ¹⁶ N. Romming, C. Hanneken, M. Menzel, J. E. Bickel, B. Wolter, K. von Bergmann, A. Kubetzka, and R. Wiesendanger, *Science* **341**, 636 (2013).
 - ¹⁷ X. Zhang, M. Ezawa, and Y. Zhou, *Sci. Rep.* **5**, 9400 (2015).
 - ¹⁸ A. Bogdanov and A. Hubert, *J. Magn. Magn. Mater.* **138**, 255 (1994).
 - ¹⁹ S. D. Yi, S. Onoda, N. Nagaosa, and J. H. Han, *Phys. Rev. B* **80**, 054416 (2009).
 - ²⁰ J. H. Han, J. Zang, Z. Yang, J.-H. Park, and N. Nagaosa, *Phys. Rev. B* **82**, 094429 (2010).
 - ²¹ M. C. Ambrose and R. L. Stamps, *New Journal of Physics* **15**, 053003 (2013).
 - ²² U. Güngördü, R. Nepal, O. A. Tretiakov, K. Belashchenko, and A. A. Kovalev, *Phys. Rev. B* **93**, 064428 (2016).
 - ²³ M. Böttcher, S. Heinze, S. Egorov, J. Sinova, and B. Dupé, *New Journal of Physics* **20**, 103014 (2018).
 - ²⁴ Y. Nishikawa, K. Hukushima, and W. Krauth, *Phys. Rev. B* **99**, 064435 (2019).
 - ²⁵ N. Mohanta, E. Dagotto, and S. Okamoto, *Phys. Rev. B* **100**, 064429 (2019).
 - ²⁶ J. H. Wernick, G. K. Wertheim, and R. C. Sherwood, *Mater. Res. Bull.* **7**, 1431 (1972).
 - ²⁷ W. Munzer, A. Neubauer, T. Adams, S. Mühlbauer, C. Franz, F. Jonietz, R. Georgii, P. Böni, B. Pedersen, M. Schmidt, A. Rosch, and C. Pfleiderer, *Phys. Rev. B* **81**, 041203 (2010).

- ²⁸ X. Z. Yu, Y. Onose, N. Kanazawa, J. H. Park, J. H. Han, Y. Matsui, N. Nagaosa, and Y. Tokura, *Nature* **465**, 4 (2010).
- ²⁹ X. Z. Yu, N. Kanazawa, Y. Onose, K. Kimoto, W. Z. Zhang, S. Ishiwata, Y. Matsui, and Y. Tokura, *Nat. Mater.* **10**, 4 (2011).
- ³⁰ H. Wilhelm, M. Baenitz, M. Schmidt, U. K. Röbler, A. A. Leonov, and A. N. Bogdanov, *Phys. Rev. Lett.* **107**, 127203 (2011).
- ³¹ K. Shibata, X. Z. Yu, T. Hara, D. Morikawa, N. Kanazawa, K. Kimoto, S. Ishiwata, Y. Matsui, and Y. Tokura, *Nat. Nanotech.* **8**, 723 (2013).
- ³² T. Tanigaki, K. Shibata, N. Kanazawa, X. Yu, Y. Onose, H. S. Park, D. Shindo, and Y. Tokura, *Nano Letters* **15**, 5438 (2015).
- ³³ S. Seki, X. Z. Yu, S. Ishiwata, and Y. Tokura, *Science* **336**, 198 (2012).
- ³⁴ B. Dupé, M. Hoffmann, C. Paillard, and S. Heinze, *Nat. Commun.* **5**, 4030 (2014).
- ³⁵ S. Heinze, K. von Bergmann, M. Menzel, J. Brede, A. Kubetzka, R. Wiesendanger, G. Bihlmayer, and S. Blgel, *Nat. Phys.* **7**, 713 (2011).
- ³⁶ A. Soumyanarayanan, M. Raju, A. L. G. Oyarce, A. K. C. Tan, M.-Y. Im, A. P. Petrovi, P. Ho, K. H. Khoo, M. Tran, C. K. Gan, F. Ernult, and C. Panagopoulos, *Nat. Mater.* **16**, 8 (2017).
- ³⁷ M. Raju, A. Yagil, A. Soumyanarayanan, A. K. C. Tan, A. Almoalem, F. Ma, O. M. Auslaender, and C. Panagopoulos, *Nat. Commun.* **10**, 696 (2019).
- ³⁸ T. Schulz, R. Ritz, A. Bauer, M. Halder, M. Wagner, C. Franz, C. Pfleiderer, K. Everschor, M. Garst, and A. Rosch, *Nat. Phys.* **8**, 301 (2012).
- ³⁹ M. Lee, W. Kang, Y. Onose, Y. Tokura, and N. P. Ong, *Phys. Rev. Lett.* **102**, 186601 (2009).
- ⁴⁰ Y. Li, N. Kanazawa, X. Z. Yu, A. Tsukazaki, M. Kawasaki, M. Ichikawa, X. F. Jin, F. Kagawa, and Y. Tokura, *Phys. Rev. Lett.* **110**, 117202 (2013).
- ⁴¹ G. Yin, Y. Liu, Y. Barlas, J. Zang, and R. K. Lake, *Phys. Rev. B* **92**, 024411 (2015).
- ⁴² P. B. Ndiaye, C. A. Akosa, and A. Manchon, *Phys. Rev. B* **95**, 064426 (2017).
- ⁴³ K. Hamamoto, M. Ezawa, and N. Nagaosa, *Phys. Rev. B* **92**, 115417 (2015).
- ⁴⁴ B. Göbel, A. Mook, J. Henk, and I. Mertig, *Phys. Rev. B* **95**, 094413 (2017).
- ⁴⁵ K. S. Denisov, I. V. Rozhansky, N. S. Averkiev, and E. Lähderanta, *Scientific Reports* **7**, 17204 (2017).
- ⁴⁶ B. Göbel, A. Mook, J. Henk, and I. Mertig, *Eur. Phys. J. B* **91**, 179 (2018).
- ⁴⁷ N. Nagaosa, *J. Phys. Soc. Jpn.* **75**, 042001 (2006).